Supporting information for:

Hot electron thermoreflectance coefficient of gold during electron-phonon nonequilibrium

Elizabeth L. Radue,[†,‡] John A. Tomko,[¶,‡] Ashutosh Giri,[†] Jeffrey L. Braun,[†] Xin Zhou,[§,‖] Oleg V. Prezhdo,[‖,⊥] Evan L. Runnerstrom,[#] Jon-Paul Maria,[#] and Patrick E. Hopkins[∗,†,¶,@]

†*Department of Mechanical and Aerospace Engineering, University of Virginia, Charlottesville, VA, USA 22904*

‡*These authors contributed equally to this work*

¶*Department of Materials Science and Engineering, University of Virginia, Charlottesville, VA, USA 22904*

§*College of Environmental and Chemical Engineering, Dalian University, Dalian, P. R. China 116622*

‖*Department of Chemistry, University of Southern California, Los Angeles, CA, USA 90089*

⊥*Department of Physics and Astronomy, University of Southern California, Los Angeles, CA, USA 90089*

#*Department of Materials Science and Engineering, North Carolina State University, Raleigh, North Carolina 27695, USA*

@*Department of Physics, University of Virginia, Charlottesville, VA, USA 22904*

E-mail: phopkins@virginia.edu

Two-temperature model (TTM)

The analysis of measured temporal dynamics in our pump-probe experiments relies on solving equations for a material's thermal response via a semi-classical two-temperature model (TTM). This TTM is based on the following description of ultrafast laser heating: The incident laser pulse couples and transfers energy directly to electrons; this energy deposition leads to a large increase in the temperature of the electronic subsystem; in doing so, the electrons are now out of equilibrium with the phonon/lattice subsystem which has not gained energy directly from the initial laser interaction. In a sufficiently thin metal film supported by a dielectric substrate, where electron transport out of the initially heated area cannot occur on rapid time scales, equilibrium is achieved through electron-phonon coupling. In thin gold films excited by femtosecond pulses, the electron and phonon subsystem temperatures reach this equilibrium on the order of a few picoseconds, after which energy is conducted by the lattice via 'typical' thermal transport.

In thin metal films, we can define the respective temporal evolution of the electron and phonon subsystem temperatures via

$$C_e(T_e)\frac{\partial T_e}{\partial t} = -G(T_e - T_p) + S(t) \tag{1}$$

$$C_p(T_p)\frac{\partial T_p}{\partial t} = G(T_e - T_p) \tag{2}$$

where C_e and C_p are the heat capacities of the electrons and phonons, respectively, and T_e and T_p are the temperatures of the electrons and phonons, respectively. The coupling constant associated with the aforementioned energy transfer between the two subsystems (the electron-phonon coupling constant) is given by G, and the source term, $S(t)$, accounts for the parameters associated with the pump pulse from the ultrafast laser. In free electron metals, the electron heat capacity is well-known to vary linearly with respect to temperature, as given by $C_e = \gamma T_e$. Here, we use a value of $\gamma = 62.9$ J m^{-3} K^{-2}. An example of these calculated temperature evolutions on ultrafast time scales is shown in Fig. S1a. As shown, there is an additional steady-state temperature rise that leads to an increase in the 'background' temperature of the system and is not time-dependent; this temperature rise is discussed in more depth in the manuscript as well as later in the Supporting Information.

As the pump pulse has a larger beam waist than that of the probe beam at the sample surface, and the thickness of the Au film is on the order of the optical penetration depth for both the pump and probe beams ($\sim 10 - 20$ nm), we simply consider the one-dimensional solution to these equations. As such, the laser heat source term, $S(t)$, for the Gaussian beam used in this work does not include a spatial dependence and can be expressed as

$$S(t) = \frac{0.94F_{abs}}{\delta t_p} \exp[-4\ln(2)(\frac{t-2t_p}{t_p})^2] \tag{3}$$

where F_{abs} is the absorbed fluence, δ is the optical penetration depth, and t_p is the pulse width. In this case, as mentioned above, the optical penetration depth is simply equated to the thickness of the Au film (16 nm). As the beam sizes were measured with both an optical beam profiler as well as via knife-edge, the absorbed fluence can be determined by setting the sample at a $\sim$5 degree angle relative to the incident beam and measuring the transmitted and reflected power of the 400 nm pump beam, then subtracting these from the incident power. Measurements regarding the pulse width are discussed in detail later in the Supporting Information.

Clearly, neither the temporal changes of the electron or phonon subsystems, nor the pump source term, account for the well-known fact that following an ultrafast optical excitation, a portion of the gold's electrons are in a non-thermal state and cannot be accurately defined by a Fermi-Dirac distribution for a few hundred femtoseconds. These non-thermalized electrons travel ballistically at approximately the Fermi velocity (on the order of 10^6 m s^{-1}). While the ballistic portion does not play a significant role at these film thicknesses, as the electrons would simply scatter and thermalize at the surface boundary rather than travel to a position below the probed optical penetration depth, these non-thermal electrons will deviate from the scattering rates discussed below.

As elucidated by recent work, the weak contribution of this non-thermal electron distribution to changes in reflectivity has essentially subsided within less than 500 fs.[S1] Additionally, this same work has shown that within 70 fs of the pump excitation, the step-like function associated with these non-thermal electrons has already reduced to half of its extension in energy-space relative to the Fermi energy. As the cross-correlation of the pulses used in our measurements is greater than the previously measured time necessary to observe changes associated with non-thermal electrons (as discussed later), and the probe pulse is over twice the duration of the observed energy reduction of 70 fs, we can approximate this electron thermalization time as simply an increase in the pulse width. In doing so, we simply substitute the sum of the values to an effective pulse width, i.e., $t_{p,eff} = t_p + t_{ee}$, where t_{ee} is the approximated electron thermalization time, which we assume to be 600 fs, thus using a value of $t_p = 800$ fs, which is the approximate cross-correlation of the pump and probe pulses in this work.

To solve these equations and determine the temperature evolution of these systems, we utilize the relationship between temperature and the dielectric function of a material as discussed in the manuscript. In short, within the Drude model, the free electron contribution to the dielectric function, ϵ, of a metal such as gold is given by

$$\epsilon = 1 - \frac{{\omega_p}^2}{\omega^2 + i\omega\tau^{-1}} \tag{4}$$

where ω is the frequency of light. The temperature dependence of this function, and thus the temperature dependence of changes in optical reflectivity, can arise from the other two parameters of this expression, ω_p and τ. As the plasma frequency, ω_p, of a metal is defined by $\omega_p = 4\pi N_e e^2/m^*$, any change in the electronic number density, N_e, or the effective mass of the contributing electrons, m^*, will clearly lead to a change in the dielectric function. As the band structure of a material is directly related to the structure of the atomic lattice, one could expect a change in effective mass for any increase in temperature, as the bond distance will increase due to thermal expansion. Similarly, as the *total* number of electrons associated with each atom is a nominal value, any variation in the

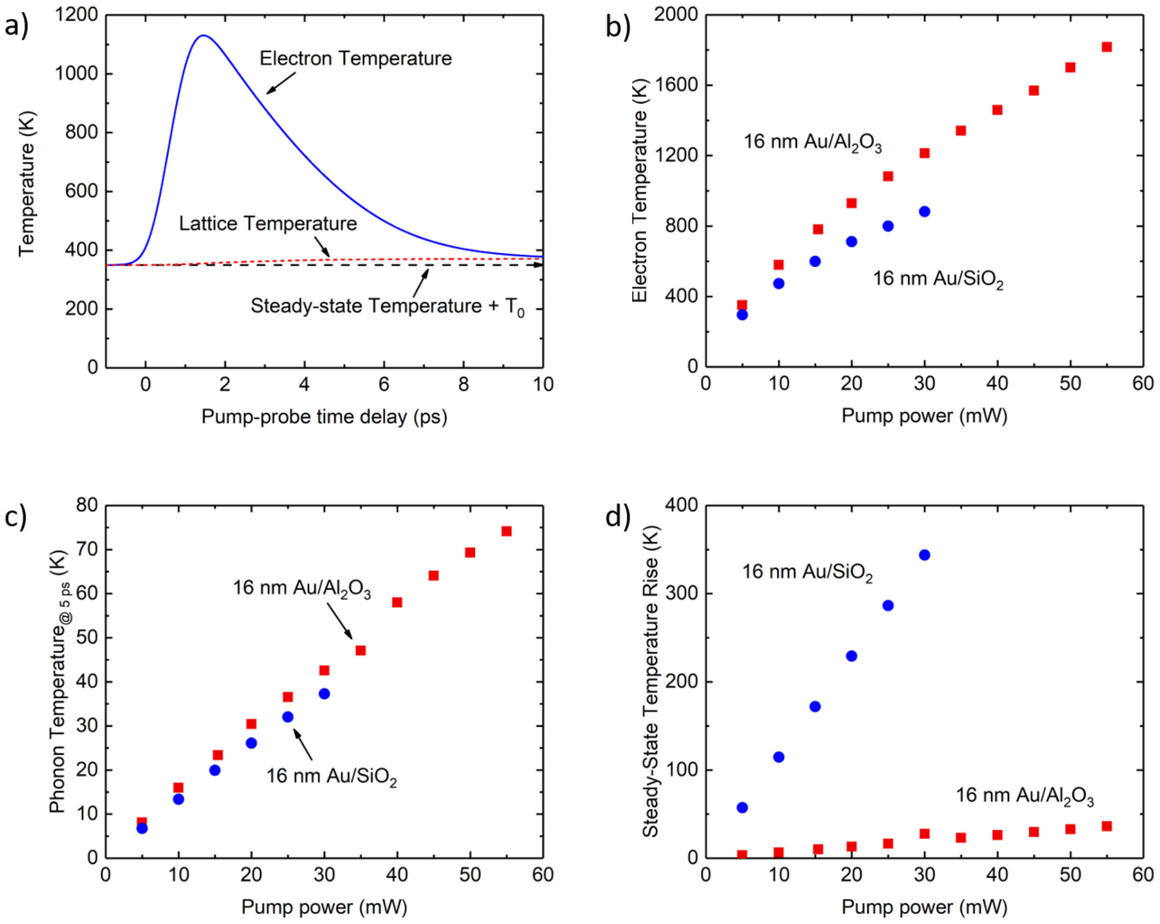

Figure S1: a) Temperature evolution of the electron and phonon subsystems following an ultrafast pump as calculated with our two-temperature model. b) Peak electron temperature and c) peak phonon temperature from TTM as a function of incident pump power for 16 nm Au on both a sapphire (red squares) and glass (blue circles) substrate. d) Steady-state temperature rise associated with the high-repetition rate oscillator used in this work as calculated by the cylindrical heat equation.

atomic spacing of the material (e.g., thermal expansion) will lead to a change in the total volume of the material; this volumetric expansion causes the electron number density, N_e, to decrease with increasing temperature. Thus, the plasma frequency's temperature dependence is directly related to thermal expansion and is given by

$$\omega_p = \frac{\omega_p(T_0)}{\sqrt{1 + 3\alpha(T_p - T_0)}} \tag{5}$$

where α is the linear thermal expansion coefficient of a given material; for Au, $\alpha = 14.2 \times 10^{-6}$ K^{-1}.

On the other hand, the scattering rate of electrons, τ, varies as a function of not only phonon/lattice temperature, but also the temperature of the electrons themselves. As discussed in the manuscript, this relaxation time is dependent on both electron-electron scattering processes as well as electron-phonon scattering. Given this, the effective scattering rate can be expressed as $\tau^{-1} = \tau_{ee}^{-1} + \tau_{ep}^{-1}$. In the case of free electrons, the dominant carriers in the case of metals such as Au, we make the common assumption that $\tau_{ee}^{-1} = A_{ee}T_e^2$ and $\tau_{ep}^{-1} = B_{ep}T_p$, where A_{ee} and B_{ep} are constants relating to the aforementioned electron-electron and electron-phonon scattering processes. These constants are assumed to have values of $A_{ee} = 1.5 \times 10^7$ K^{-2} and $B_{ep} = 1.7 \times 10^{11}$ K^{-1} for all TTM calculations in this work, unless noted otherwise; these values are in agreement with previous literature values and our dR/R analysis performed at a time delay of 500 ps, as discussed in detail later.

To directly compare the accuracy of our dR/dT_e derivation/expansion from the manuscript with TTM calculations, we do not include the temperature dependence associated with the plasma frequency in our model. To validate this simplification, we can consider the following: if we assume an arbitrary 100 K increase in temperature from ambient conditions ($\sim$300 K) and use the values referenced in the previous paragraph, we see that the plasma frequency varies by $\sim 2\%$, whereas the scattering rate changes by nearly 34%. Additionally, this assumption relies on an equivalent increase in both the electron and phonon temperatures of the system; the majority of our work is focused on the case of non-equilibrium distributions, where the electron temperature is much greater than the lattice temperature (i.e., $T_e >> T_p$). At the peak electron temperature rise, where dR/dT_e is analyzed, the lattice contribution to changes in reflectivity is negligible as the electrons have not yet coupled to phonons and thus have not transferred energy to the lattice, and the change in reflectivity would be dominated solely by the electron-electron scattering rate as it is the only T_e-dependent variable.

While the addition of a temperature dependent plasma frequency does not alter the peak electron temperature, and thus does not affect the results surrounding the non-equilibrium thermoreflectance coefficient reported here, and also does not significantly affect our data analysis at 500 picoseconds (i.e., when $T_e \approx T_p$) and the associated extraction of the parameters (A_{ee} and B_{ep}), we do note that its inclusion in the TTM would drastically affect other works that aim to determine electron-phonon coupling constants via analysis of the time-constant associated with the ultrafast decay over the first few picoseconds. As shown in Fig. S2, the addition of a temperature-dependent plasma frequency when extracting B_{ep} negligibly alters the best-fit.

Note, certain experimental configurations can obtain varying sensitivities to the scattering coefficients, τ_{ee} and τ_{ep}, and thus the temperature dependence of ω_p, and hence produce differing results for the reported thermoreflectance coefficient. For example, in the case of infrared reflectivity/absorption measurements where the lattice temperature and electron temperature are not separated (i.e., equilibrium is assumed), and the photon energy is much less than the energy required to induce an interband transition, one can typically neglect the temperature dependence associated with electron-electron scattering and thus only be dependent upon the lattice temperature (e.g., $\tau^{-1} \approx C \cdot B_{ep} T_p$, where C is a temperature-independent constant related to the e-e scattering rate). Conversely, in the case where the electronic subsystem temperature is in a state of non-equilibrium relative to the lattice temperature (i.e., $T_e >> T_p$), Fermi-smearing occurs and the width of the electron distribution is greatly increased. Although the interband transition threshold under equilibrium conditions is $\sim$2.55 eV in Au, when the electron temperature is sufficient to create holes $\sim$1 eV beneath the Fermi energy, a photon energy of only $\sim$1.55 eV is necessary to transition a d-band electron to near Fermi surface holes. In this case, where near-infrared light, such as the 800

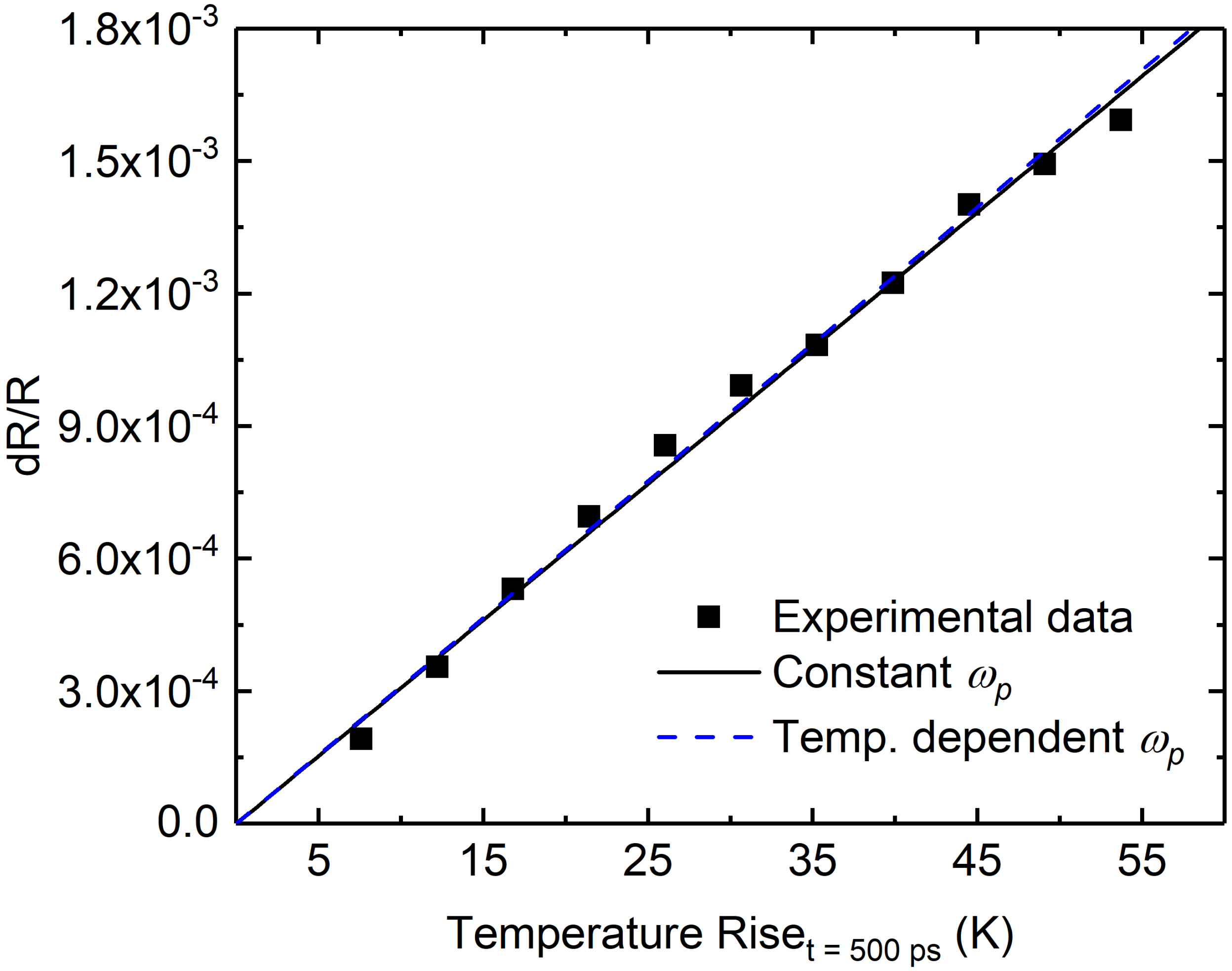

Figure S2: Fit of the temperature-dependent dielectric function for extraction of B_{ep} with (black line) and without (blue dashed line) a temperature-dependent plasma frequency, ω_p, to our experimentally measured dR/R as a function of the calculated temperature at 500 ps; $B_{ep} = 2.11 \times 10^{11}$ K^{-1} in both cases.

nm probe beam ($\sim$1.55 eV), can induce such a transition, its reflectivity becomes highly-dependent on the width of the Fermi-Dirac distribution, and thus highly-dependent on electron temperature. Of course, this 1 eV 'smearing' only occurs at near-melting temperatures for such metals should the electron and lattice have equivalent temperatures, and is why it is only observed under such non-equilibrium conditions when $T_e \gg T_p$. Nonetheless, given the electron temperatures and probe wavelength used in this work, we gain a sensitivity to the electron temperature and the e-e scattering rate associated with it. Attempting to remove this temperature dependence creates an inability to accurately describe the experimental decay curves shown in this work, as shown in the manuscript.

Physically, this electronic scattering rate can be derived from Fermi liquid theory, whereby the relaxation rate is inversely proportional to the square of a given electron's energy relative to the Fermi energy, or $\tau_{ee} = \tau_0(E_F/\Delta E)^2$, where ΔE is simply $(E_{electron} - E_F)$, and τ_0 is an intrinsic proportionality constant.[S2] Under this approximation, the aforementioned Fermi-smearing at elevated temperatures leads to an increased electron population and increased number of hole states above and below the Fermi energy, respectively; the width of this 'smearing' is approximately $\sim 2k_BT_e$ about E_F. Clearly, this creates a number of electrons with $\Delta E \propto T_e$, and thus leads to a scattering time of $\tau_{ee} \propto {T_e}^{-2}$. While one may consider that the classical picture of the Drude model does not explicitly account for electron-electron interactions, a number of works, particularly the seminal review by Kaveh and Wiser,[S3] have determined that electron-electron scattering does in fact play a role when considering optical frequencies. This apparent discrepancy can be considered from the fact that the classical Drude model relies on translational symmetry of the electron gas, where local momentum is conserved during electron-electron scattering processes, hence the model's typical dependence on electron-ion scattering. However, non-spherical Fermi surfaces, higher momentum bands than the nearly-free electron sp-band of Au (i.e., d-band electrons), and perturbations of the electron gas (e.g., short-pulse laser interactions) break this invariance and localized momentum exchange due to electron correlations must be considered; these phenomena are clearly not considered in the classical Drude model.

We numerically solve these equations using an iterative fourth-order Runge-Kutta method, and fit the electron-phonon coupling constant, G, via non-linear least squares fitting. Although G is the fitted-variable, the large sensitivity to A_{ee} and B_{ep} from this model creates a clear lack of agreement between the model and experimental results when there is more than 5% deviation from the values reported here. The peak electron temperature, occurring at $t = 0$, that is used for our reported values of dR/dT_e, along with the maximum phonon temperature, which occurs just after electrons couple to the lattice, that has been calculated via this TTM approach as a function of incident pump power is shown in Fig. S1b and c, respectively.

Determination of lattice temperature rise via heat diffusion

While we use the two-temperature model to determine the single-pulse temperature rise when electrons and phonons are out of equilibrium with one another, to calculate the lattice temperature rise at times far after electron relaxation ($t > 100$ ps), we model the temperature rise via the heat diffusion equation. This approach is used to estimate the modulated temperature rise at 500 ps used to determine the thermoreflectance coefficient, as well as the steady-state temperature rise that results from accumulation of heat between pulses. Because the laser beam is Gaussian, it is convenient to solve the radially symmetric form of the heat diffusion equation, given by

$$\kappa_{\mathrm{r}} \left\{ \frac{1}{r} \frac{\partial T(z,r,t)}{\partial r} + \frac{\partial^2 T(z,r,t)}{\partial r^2} \right\} + \kappa_{\mathrm{z}} \frac{\partial^2 T(z,r,t)}{\partial z^2} = C_{\mathrm{v}} \frac{\partial T(z,r,t)}{\partial t}, \tag{6}$$

where κ_{r} and κ_{z} are in-plane and cross-plane thermal conductivity, respectively, T is the lattice temperature rise, r is the radius, z is the depth, C is the volumetric heat capacity of the lattice, and t is the time. We treat the laser heat flux as a surface boundary condition, together with a semi-infinite boundary condition in z and r to solve for the temperature rise at the sample surface. Furthermore, we integrate the radial surface temperature rise induced by the pump over the Gaussian intensity of the probe to obtain a single temperature rise corresponding to the detected change in reflectance. The solution is derived in our previous work,[S4] but we include the relevant equations below. In short, the probe averaged surface temperature rise resulting from a pulsed laser heat source modulated at angular frequency ω_0 is

$$T_{\mathrm{top}} = \frac{A_0}{2\pi} \int_0^\infty \sum_{n=-\infty}^{\infty} \left(-\frac{D}{C}\right)_{\omega=\omega_0+n\omega_s} \exp\left(-\frac{k^2(r_0^2+r_1^2)}{8}\right) \mathrm{e}^{i(\omega_0+n\omega_s)t} k \, \mathrm{d}k, \tag{7}$$

where A_0 is the absorbed power from the pump heating, $\omega_s/2\pi$ is the repetition rate of the laser, and r_0 and r_1 are the pump and probe radii, respectively. D and C define the thermal properties of the sample; in this case we use a two-layer model including the gold film layer and bulk substrate, so that

$$C = -q_2\kappa_{\mathrm{z},2} - q_1\kappa_{\mathrm{z},1} \tanh\left(q_1 L_1\right) \left(\frac{q_2\kappa_{\mathrm{z},2}}{h_{\mathrm{k}}} + 1\right) \tag{8}$$

$$D = 1 + q_2\kappa_{\mathrm{z},2} \left(\frac{1}{q_1\kappa_{\mathrm{z},1}} \tanh\left(q_1 L_1\right) + \frac{1}{h_{\mathrm{k}}}\right) \tag{9}$$

where subscripts indicate layer number and coordinate direction and L_1 is the thickness of the gold film. q is defined by

$$q_{\mathrm{j}}^2 = \frac{1}{\kappa_{\mathrm{z,j}}}(i\omega C_{\mathrm{v,j}} + \kappa_{\mathrm{r,j}}k^2). \tag{10}$$

The thermal parameters used for calculation are given in Table S1 for Au, Al_2O_3, and SiO_2. Heat capacities were assumed as literature values[S5,S6] while thermal conductivities were determined experimentally; for Au, 4-point probe resistivity measurements were used and TDTR was used to measure both thermal conductivity of the substrates and thermal boundary conductance across the Au/substrate interfaces.

For steady-state temperature rise measurements, the same heat diffusion equation is used, but the heat source is changed to an equivalent CW source with $\omega_0 = 0$ and having the absorbed power A_0. In practice, this simplifies Eq. 7 to

$$T_{\mathrm{SS}} = \frac{A_0}{2\pi} \int_0^\infty \frac{-D(k,0)}{C(k,0)} \exp\left(-\frac{k^2(r_0^2 + r_1^2)}{8}\right) k \, \mathrm{d}k. \tag{11}$$

The results from these steady-state temperature rise calculations are shown in Fig. S1d as a function of the incident pump power.

Table S1: Room temperature thermal parameters used in calculating temperature rises in this study. κ_{r} is thermal conductivity in the radial (in-plane) direction, κ_{z} is thermal conductivity in the z (out-of-plane) direction, C is volumetric heat capacity, and $h_{\mathrm{Au/x}}$ is the thermal boundary conductance between Au and the substrate.

Material	κ_{z} (W m^{-1} K^{-1})	κ_{r} (W m^{-1} K^{-1})	C (J cm^{-3} K^{-1})	$h_{\mathrm{Au/x}}$ (MW m^{-2} K^{-1})
SiO_2	1.35	1.35	1.66[S5]	50
Al_2O_3	35	35	3.06[S5]	50
Au	102	102	2.49[S6]	-

Picosecond acoustics

To determine the thickness of the Au films used in this work, we rely on an inherent aspect of ultrafast pump probe measurements: picosecond acoustics. In such experiments, the intense pump pulse induces a large temperature rise within the optical absorption depth of the Au film. This rapid temperature rise leads to a thermo-elastic stress in the film that launches a coherent acoustic phonon through the metal film towards its supporting substrate. When this acoustic wave reaches the film/substrate interface, it is partially transmitted into the substrate, but also partially reflected back towards the surface of the metal film; as this acoustic wave is essentially a density perturbation within the metal transducer, it leads to a change in the dielectric function/refractive index that can be observed by the probe laser pulse upon arrival at the film surface. As Au has a well-known longitudinal phonon velocity (i.e., sound speed), one can determine the thickness of the metal film, d, from the round-trip period associated with this acoustic wave by the propagation speed of a coherent acoustic phonon by[S7]

$$d = \frac{\tau v_{acoustic}}{2} \tag{12}$$

where τ is the period of the observed change in reflectivity and $v_{acoustic}$ is the velocity of the longitudinal wave in the metal film; the factor of $1/2$ corresponds to the fact that the acoustic wave is only observed on the probed surface and must traverse the metal film twice before it is detected.

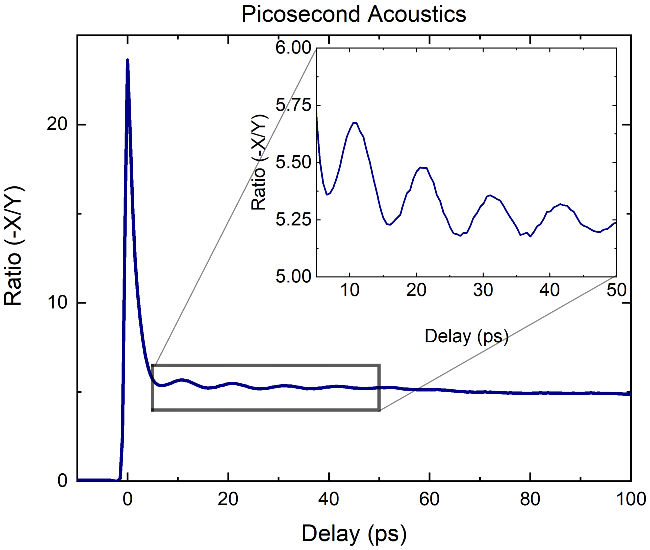

Figure S3: Time-domain thermoreflectance (TDTR) data showing the periodic arrival of the pump-induced pressure front on the surface of our thin Au film on a sapphire substrate. The period of these oscillations is measured to be ~10 picoseconds, corresponding to an Au film thickness of 16 nm.

An example of these picosecond acoustic measurements can be seen in Fig. S3, where a periodic change in reflectivity of the Au film is observed every ~10 ps due to the arrival of this pressure front at the surface of the film. Using a sound speed, $v_{acoustic}$, of 3240 m s^{-1} for Au, the thickness of the metal film is calculated to be 16 nm, which is in excellent agreement with the thickness obtained from XRR; the results from XRR are discussed later in the Supporting Information. Note, Fig. S3 shows the ratio of the in-phase signal from our lock-in amplifier, X, to the out-of-phase signal, Y, as a function of time. At these time scales, the in-phase signal contains the magnitude of change in reflectivity due to heating from the pump-pulse, whereas the temporal change in the out-of-phase signal due to lattice temperature changes over this time delay is minor. Hence, in taking the ratio of these values, electronic noise can be ‘normalized‘ out of the signal to provide a more accurate representation of these acoustic oscillations.

Pulse width and cross correlation of pulses

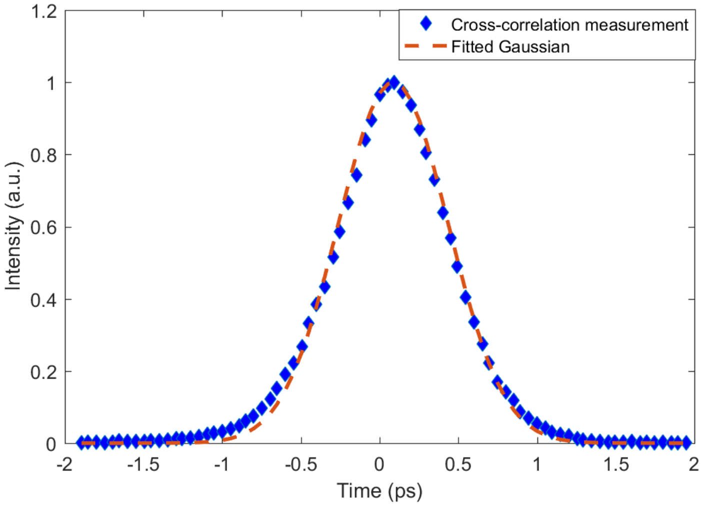

Figure S4: Measured second harmonic generation intensity of the pump and probe pulses as a function of the temporal offset between the two pulses. The FWHM of this cross-correlation is measured to be 824 ± 20 femtoseconds.

The pulse width of the 800 nm probe pulses were measured via the Frequency Resolved Optical Gating (FROG) technique. This technique relies on splitting the probe pulse into two temporally-separated paths that are focused into a second harmonic generation (SHG) medium and measuring the SHG intensity as a function of the temporal offset between the two pulses. In doing so, we determine the probe pulse has a temporal FWHM of 220 ± 20 femtoseconds. As our pump pulse is already frequency-doubled to 400 nm before arrival at the sample surface and is thus greatly reduced in intensity, this process cannot be repeated for measurement of the pump beam’s pulse width. The cross-correlation of the pump and probe pulses were measured in a similar fashion, where a BBO crystal is used as the third harmonic generation medium via spatial and temporal overlap of the 800 and 400 nm pulses at zero incidence. By adjusting the delay between the pump and probe, we can obtain the cross-correlation of the two pulses; as shown in Fig. S4, the cross-correlation of the pump and probe pulses is measured to have a FWHM of 824 ± 20 femtoseconds.

XRD and XRR experimental method

As mentioned in the main text, X-ray diffraction and reflectivity patterns were collected using a PANalytical Empyrean XRD in parallel beam geometry with a Ge (220) double-bounce hybrid mirror-monochromator (1/32° divergence slit) incident optic and a 0.18° parallel plate collimator and proportional detector (Xe) as receiving optics.

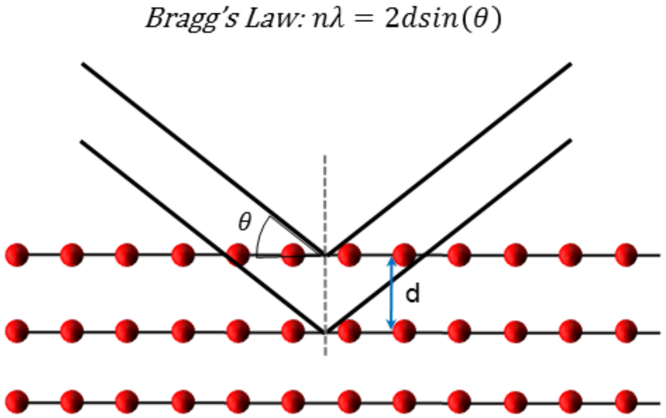

Figure S5: Principle behind XRD measurements: as x-rays reflect off of planes within a crystalline material, they will constructively or destructively interfere based on the angle of incidence and the spacing of the planes.

Figure S5 shows how we can back out plane dimensions through $\theta - 2\theta$ measurements in crystalline materials, through diffracting x-rays off of crystalline planes. The spacing of the planes is determined by Braggs law, and by knowing the angles in which the x-rays constructively interfere, we can determine the spacing of the crystalline planes. More pertinent to our measurements, we can also look at the shift in the diffraction peak, and back out effects from strain and grain sizes from the position and width of the peak. Figure S6 shows the set up for a XRD stage measuring diffraction of a thin film sample. $\theta - 2\theta$ scans measure the in-plane crystallinity, as both the source and the detector sweep over the range together. By rotating χ we can measure in plane peaks, and by rotating ϕ we can determine the epitaxy of the film and the number of crystalline orientations. Figure S7 shows the X-Ray Reflectivity (XRR) measurements of the films.

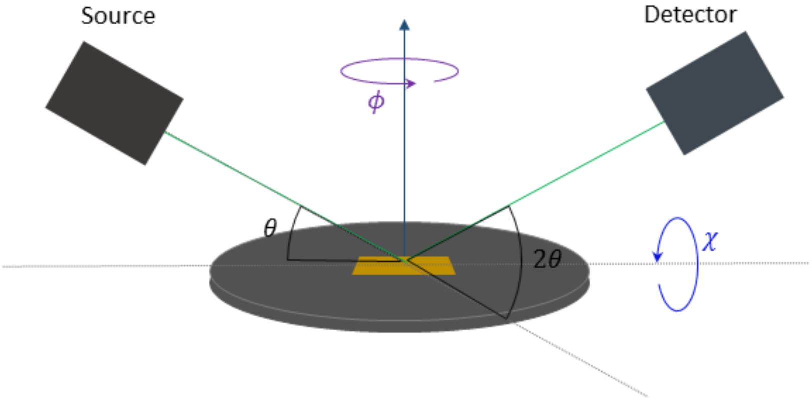

Figure S6: $\theta - 2\theta$ measurement set-up for XRD of a thin film.

X-Ray reflectivity (XRR) measurements are taken at very low angles of θ. For a thin film, the resulting intensity at the detector will be modulated from interference from the film interfaces. This relationship can be determined by

$$d \approx \frac{\lambda}{2} \frac{1}{\theta_{m+1} - \theta_m} \tag{13}$$

where λ is the beam's wavelength, and $\theta_{m+1} - \theta_m$ is the spacing between fringes. As can be seen in Figure S7, the thinner the film, the bigger the fringes.

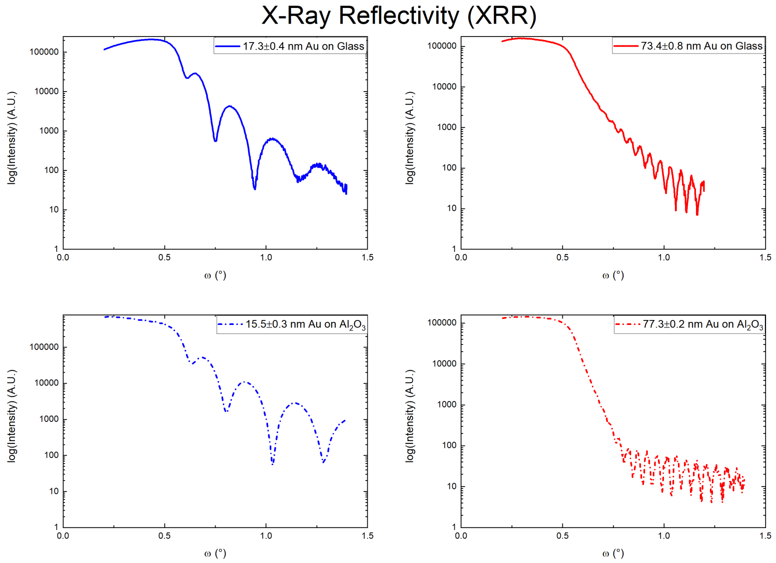

Figure S7: XRR data for Au films in this study. From this we can determine the thicknesses of the films for our thermal modeling.

Complex coefficients of Equation 4 in the main manuscript

In the main manuscript, we show that the expansion of dR/dT_e about T_e and T_p yields

$$\frac{dR}{dT_e} \approx \sqrt{R}\left(\tilde{C} + \tilde{D}T_p\right)T_e \tag{14}$$

where $\tilde{C}$ and $\tilde{D}$ are given by

$$\tilde{C} = -\frac{4iA_{ee}\omega_{\text{plasma}}^2}{\omega^3\sqrt{1-\frac{\omega_{\text{plasma}}^2}{\omega^2}}\left(1+\sqrt{1-\frac{\omega_{\text{plasma}}^2}{\omega^2}}\right)^2} \tag{15}$$

and

$$\tilde{D} = -\frac{1}{\omega}4iA_{ee}\omega_{\text{plasma}}^2\left(\tilde{D}_1 + \tilde{D}_2 + \tilde{D}_3\right) \tag{16}$$

where

$$\tilde{D_1} = -\frac{iB_{ep}\omega^2_{\text{plasma}}}{\omega^5\left(1-\frac{\omega^2_{\text{plasma}}}{\omega^2}\right)\left(1+\sqrt{1-\frac{\omega^2_{\text{plasma}}}{\omega^2}}\right)^3} \tag{17}$$

$$\tilde{D_2} = -\frac{1}{\left(1+\sqrt{1-\frac{\omega^2_{\text{plasma}}}{\omega^2}}\right)^2}\left(\frac{iB_{ep}\omega^2_{\text{plasma}}}{2\omega^5\left(1-\frac{\omega^2_{\text{plasma}}}{\omega^2}\right)^{3/2}}+\frac{2iB_{ep}}{\omega^3\sqrt{1-\frac{\omega^2_{\text{plasma}}}{\omega^2}}}\right) \tag{18}$$

$$\tilde{D_3} = -\frac{iB_{ep}\omega^2_{\text{plasma}}\sqrt{\frac{\omega^2-\omega^2_{\text{plasma}}}{\omega^2}}}{\omega^3\left(\omega^2-\omega^2_{\text{plasma}}\right)\sqrt{1-\frac{\omega^2_{\text{plasma}}}{\omega^2}}\left(1+\sqrt{1-\frac{\omega^2_{\text{plasma}}}{\omega^2}}\right)^4} \tag{19}$$

References

(S1) Heilpern, T.; Manjare, M.; Govorov, A. O.; Wiederrecht, G. P.; Gray, S. K.; Harutyunyan, H. Determination of hot carrier energy distributions from inversion of ultrafast pump-probe reflectivity measurements. *Nature Communications* **2018**, *9*.

(S2) Fann, W. S.; Storz, R.; Tom, H. W. K.; Bokor, J. Electron thermalization in gold. *Physical Review B* **1992**, *46*, 13592–13595.

(S3) Kaveh, M.; Wiser, N. Electron-electron scattering in conducting materials. *Advances in Physics* **1984**, *33*, 257–372.

(S4) Braun, J. L.; Hopkins, P. E. Upper limit to the thermal penetration depth during modulated heating of multilayer thin films with pulsed and continuous wave lasers: A numerical study. *Journal of Applied Physics* **2017**, *121*, 175107.

(S5) Touloukian, Y. S.; Powell, R. W.; Ho, C. Y.; Klemens, P. G. *Thermophysical Properties of Matter - Specific Heat: Nonmetallic Solids*; New York, IFI/Plenum, 1970; Vol. 5.

(S6) Touloukian, Y. S.; Powell, R. W.; Ho, C. Y.; Klemens, P. G. *Thermophysical Properties of Matter - Thermal Conductivity: Nonmetallic Solids*; New York, IFI/Plenum, 1970; Vol. 2.

(S7) Thomsen, C.; Maris, H. J.; Tauc, J. Picosecond acoustics as a non-destructive tool for the characterization of very thin films. *Thin Solid Films* **1987**, *154*, 217–223.